The influence of negative ions in helium–oxygen barrier discharges: III. Simulation of laser photodetachment and comparison with experiment

Sebastian Nemschokmichal, Robert Tschiersch and Jürgen Meichsner

Institute of Physics, University of Greifswald, Felix-Hausdorff-Str. 6, D-17489 Greifswald, Germany

E-mail: nemschok@physik.uni-greifswald.de

CrossMark

Abstract

The laser photodetachment experiment in a diffuse helium–oxygen barrier discharge is evaluated by a 1D fluid simulation. As in the experiment, the simulated discharge operates in helium with 400 ppm oxygen admixture at 500 mbar inside a discharge gap of 3 mm. The laser photodetachment is included by the interaction of negative ions with a temporally and spatially dependent photon flux. The simulation with the usually applied set of reactions and rate coefficients provides a much lower negative ion density than needed to explain the impact on the discharge characteristics in the experiment. Further processes for an enhanced negative ion formation and their capabilities of reproducing the experimental results are discussed. These further processes are additional attachment processes in the volume and the negative ion formation at the negatively charged dielectric. Both approaches are able to reproduce the measured laser photodetachment effect partially, but the best agreement with the experimental results is achieved with the formation of negative ions at the negatively charged dielectric.

1. Introduction

Discharges operating in helium–oxygen gas mixtures are widely used for applications at atmospheric pressure [1–3]. Helium lowers the power requirements, whereas oxygen serves as the source of radicals. One common discharge type at atmospheric pressure, operating occasionally in helium-oxygen gas mixtures, is the dielectric barrier discharge [4–6]. The charge accumulation on the dielectrics during the electric breakdown is a characteristic trait of the barrier discharge, which causes a self-extinction of the discharge and keeps the gas temperature low. The latter is important for the treatment

of heat-sensitive materials, for instance, in biology and medicine.

Since oxygen is strongly electronegative, the use of oxygen results in the formation of negative ions by electron attachment in the volume, which reduces the effective ionization rate. Furthermore, the additional ion-ion-recombination enhances the total recombination rate. In the case of dielectric barrier discharges, the electron attachment might retard the discharge breakdown, whereas the enhanced recombination rate should shorten the afterglow. In this context, the formation of negative ions might be responsible for the transition from the diffuse to the filamentary discharge mode when adding oxygen to helium [7].

The common way to measure the density of negative ions is to detach the negative ions by laser photons and to measure the corresponding change in electron density by probe measurements [8] or microwave interferometry [9]. For the

1
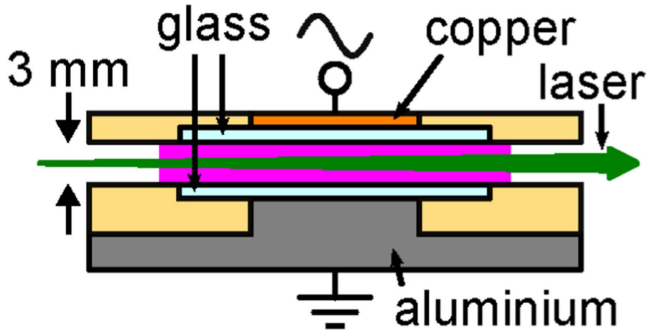
Figure 1. Sketch of the laser photodetachment experiment.

Figure 2. Experimentally observed influence of the laser photo-detachment of negative ions on the discharge development: gap voltage U_{gap} and discharge current I_{dis} without the laser (gray solid lines) and with laser photodetachment (blue, red dashed lines) depending on time. The highlighted area marks the time window where the laser effects the discharge breakdown. Reproduced from [11]. © IOP Publishing Ltd. All rights reserved.

dielectric barrier discharge, both methods are inappropriate because of the atmospheric pressure and the small dimensions of the discharge configuration. However, it was possible to perform a laser photodetachment experiment in a diffuse helium–oxygen barrier discharge [10], and to observe the changes in discharge behavior by the released electrons instead of measuring the change in electron density directly. These experiments revealed an effect on the discharge development when the laser detaches the negative ions during the pre-phase of the discharge, only. Furthermore, it could be pointed out that the O^- and/or the O_3^- ions are the predominant negative ions, whereas O_2^- ions are of minor importance. To study the influence of negative ions on the discharge in more detail and to get absolute number densities a 1D fluid simulation was developed in [11]. This simulation showed that the production of negative ions by electron attachment in the volume is too low to have an influence on the discharge development for the investigated conditions. However, even if there is no influence on the discharge, the negative ion density might be large enough to cause the change in discharge after the laser photodetachment. Hence, it is necessary to simulate the laser photodetachment experiment as well to draw further conclusions. This is presented in this paper. It starts with a summary of the laser photodetachment experiment from [10] in section 2. The description of the main features of the discharge simulation from [11] and the implementation of the laser photodetachment is presented in section 3. Afterwards, the simulated laser photodetachment effect on the discharge is presented and compared to the experiment in section 4.

2. Laser photodetachment experiment

The laser photodetachment experiment is described and discussed in detail in [10], wherefore this section gives only a brief overview of this experiment. As sketched in figure 1, the laser photodetachment experiment is performed in a plane-to-plane barrier discharge configuration, consisting of a copper electrode on top and an aluminium electrode at the bottom, both covered with 0.7 mm thick glass plates at a distance of $g = 3$ mm. The discharge which is discussed here operates in helium with 400 ppm oxygen admixture at 500 mbar. It is driven by a sinusoidal voltage at a frequency of 2 kHz and an amplitude of 700 V. Under these conditions, the discharge is laterally homogeneous and operates in the glow-like discharge mode.

For the laser photodetachment experiment, a frequency doubled Nd:YAG laser beam (532 nm) is guided through the discharge in lateral direction. Its vertical extent is about 1 mm in the discharge center and it is movable in the axial direction. The general influence of the laser photodetachment on the discharge development is shown in figure 2. As visible, the laser photo-detachment during the pre-phase causes a lower breakdown voltage, which results in an earlier discharge ignition and an earlier discharge current pulse minimum as well. Furthermore, the total number of transported charges, which is the area under the discharge current pulse, is lower for the laser affected discharge. Overall, the laser photodetachment effect occurs only when the laser is fired during the pre-phase of the discharge, which is marked by the highlighted area in figure 2.

3. Setup of the simulation

3.1. Simulation of the discharge

The simulation of the discharge is the same as discussed in detail in [11], hence, only the main features are summarized in the following. Since the experimentally observed discharge is laterally homogeneous, a 1D fluid simulation is sufficient. In particular, this allows to calculate the electric field analytically from the surface charges on the dielectrics and the space charges in the gap. The helium and oxygen background gas densities are calculated by the ideal gas law, wherein the gas temperature T_{gas} is constant between 300 and 350 K. The other included neutral species are the helium metastable He^m, the helium dimer He_2, the oxygen metastable states $O_2(a^1\Delta_g)$ and $O_2(b^1\Sigma_g^+)$, the oxygen atom O with its excited states $O(^1D)$ and $O(^1S)$, and the ozone molecule O_3. These neutral species diffuse along the axial direction and become de-excited at the dielectric surfaces with a probability of 1 (He^m, He_2, $O(^1D)$, $O(^1S)$) and 0.01 (O, $O_2(a^1\Delta_g)$, $O_2(b^1\Sigma_g^+)$, O_3). The included charged species are the electrons e^-, the helium ion He^+, the helium dimer ion He_2^+, the positive oxygen ions O^+, O_2^+, and O_4^+ as well as the negative ions O^-, O_2^-, and O_3^-. The charged species are allowed to drift and diffuse in axial direction and become fully absorbed (electrons) and neutralized (ions) at the dielectric surfaces. Besides

these species, UV photons are considered as a source of secondary electrons at the dielectric surfaces, only.

The electron transport parameters (diffusion coefficient, mobility, thermal velocity) and mean electron energy are calculated using BOLSIG+ [12, 13] (default settings, except gas temperature of 350 K) and the cross sections given in the Lisbon database at lxcat.net [14]. This procedure bases on the validity of the local field approximation for atmospheric pressure discharges developing in the microsecond time scale. As well, BOLSIG+ is used to calculate the rate coefficients for several electron impact collisions. These are complemented by the reactions given in [15] to address the oxygen chemistry.

The drift-diffusion equations are solved by the explicit Euler method with variable time steps for slow, intermediate, and fast processes. For the discretization of the drift fluxes, an upwind scheme is used, whereas a centered scheme was taken for the discretization of the diffusion flux. The starting conditions for the simulations presented here are taken from the long-time simulations, so the steady state of the discharge is already reached before the laser photodetachment.

3.2. Simulation of laser photodetachment

The laser photodetachment of negative ions is implemented in the simulation by defining a number density of laser photons from the laser cross section area $A_{lsr} = a_{lsr}b_{lsr} = 1 \text{ mm} \times 6 \text{ mm}$ and the laser pulse energy E_{lsr}. Since the simulation is one-dimensional only, the included cross section area of the laser beam is rectangular and not elliptically as in the experiment. The one-dimensionality implies that the laser extension in the lateral direction equals the lateral extension of the discharge in the simulation, which is not the case in the experiment. This might result in deviations from the experiment when looking at the dependence of the laser photodetachment effect on the laser pulse energy.

To include the laser photodetachment as simple as possible in the already existing numerics, the density of laser photons

$$n_{lsr}(t, z) = \Gamma_{lsr}(t, z)/c_0 = \frac{1}{c_0}\frac{E_{lsr}\lambda_{lsr}}{c_0 h}\frac{1}{b_{lsr}}f_{lsr}(t)g_{lsr}(z) \quad (1)$$

is calculated. It depends on the flux of laser photons Γ_{lsr} and the speed of light c_0. The flux is calculated from the laser pulse energy E_{lsr}, the laser wavelength λ_{lsr}, Planck's constant h, the laser extension in the lateral direction $b_{lsr} = 6$ mm, and two functions $f_{lsr}(t)$ and $g_{lsr}(z)$ describing the distribution of the laser intensity over time and along the axial direction, respectively. The dependence in time is given by a Gaussian function

$$f_{lsr}(t) = \frac{\sqrt{4\ln2}}{T_{lsr}\sqrt{\pi}}\exp\left(-4\ln2\frac{(t - t_{lsr})^2}{T_{lsr}^2}\right) \quad (2)$$

with a laser pulse duration of $T_{lsr} = 10$ ns. This smooth function is chosen to stabilize the numerics, because the analytical calculations in [10] show that the actual temporal shape of the laser pulse is unimportant if the laser pulse
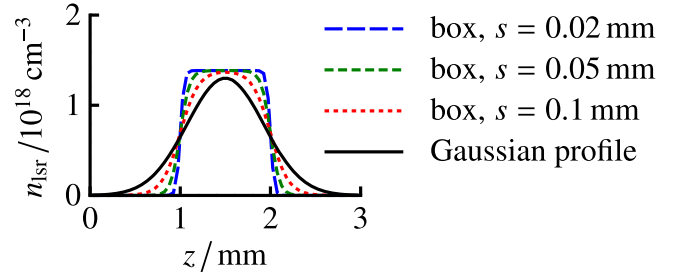
Figure 3. Spatially resolved density of laser photons at the moment t_{lsr} for different laser profiles ($z_{lsr} = 1.5$ mm, $E_{lsr} = 100$ mJ).

Table 1. Photodetachment and photodissociation cross sections for negative oxygen ions using the laser wavelength of $\lambda_{lsr} = 532$ nm.

Reaction	$\sigma \times \text{cm}^{-2}$	Reference
$O^- + hc_0/\lambda_{lsr} \rightarrow O + e^-$	6.4×10^{-18}	[16, 17]
$O_2^- + hc_0/\lambda_{lsr} \rightarrow O_2 + e^-$	1.2×10^{-18}	[17]
$O_3^- + hc_0/\lambda_{lsr} \rightarrow O_3 + e^-$	0.2×10^{-18}	[18, 19]
$O_3^- + hc_0/\lambda_{lsr} \rightarrow O_2 + O^-$	3.5×10^{-18}	[20]

duration is significantly shorter than the discharge development on the microsecond time scale. For the spatial distribution $g_{lsr}(z)$, different profiles such as a Gaussian laser beam profile

$$g_{lsr}(z) = \frac{\sqrt{4\ln2}}{a_{lsr}\sqrt{\pi}}\exp\left(-4\ln2\frac{(z - z_{lsr})^2}{a_{lsr}^2}\right) \quad (3)$$

and smoothed box profiles

$$g_{lsr}(z) = \frac{1}{a_{lsr}}\frac{1}{1 + \exp\left(\frac{z - z_{lsr} - a_{lsr}/2}{s}\right)}\frac{1}{1 + \exp\left(\frac{-z + z_{lsr} - a_{lsr}/2}{s}\right)} \quad (4)$$

are considered due to the unknown profile in the experiment. All profiles have a full width at half maximum of $a_{lsr} = 1$ mm. The smoothing of the box profiles is varied from $s = 0.1$ mm to $s = 0.02$ mm. A comparison of the spatially resolved photon densities obtained from these four different profiles at $t = t_{lsr}$ is shown in figure 3. The smoothing of the box profiles with increasing s causes a larger photon density in the wings away from the center, approaching the Gaussian profile. For most discussions, only the box profile with $s = 0.1$ mm is used, because most dependencies are the same for the different profiles. Where necessary, the influence of the different profiles is discussed. As in the experiment, the laser firing time t_{lsr} is varied in steps of microseconds, the laser position z_{lsr} from 0.5 to 2.5 mm and the laser pulse energy from zero to 100 mJ.

The photodetachment reactions are included in the calculation by rate coefficients of $k = \sigma c_0$ using the cross sections given in table 1. Besides the photodetachment, the table includes the photodissociation of O_3^-, which has a much larger cross section than the photodetachment of O_3^-.
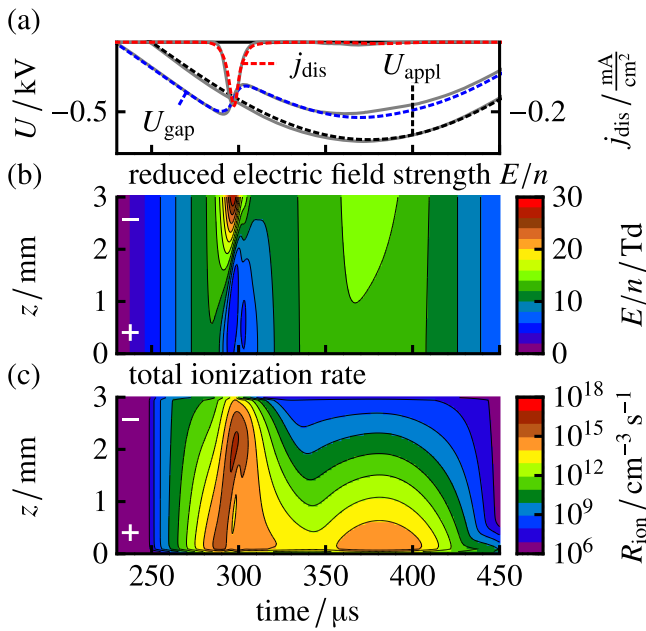
Figure 4. Discharge overview (without laser photodetachment): (a) simulated applied voltage, gap voltage, and discharge current density (colored, dashed lines) in comparison to the experiment (gray, solid lines). (b) Simulated reduced electric field strength and (c) simulated total ionization rate.

Figure 5. Change in negative charges by laser photodetachment: (a) spatially averaged densities and spatio-temporally resolved density of (b) O^- ions and (c) electrons (box-shaped laser beam profile, $z_{lsr} = 1.5$ mm, $s = 0.1$ mm, $t_{lsr} = 278$ μs, $E_{lsr} = 100$ mJ).

4. Results and discussion

4.1. Discharge characterization

To enable a quantitative comparison of the simulated laser photodetachment with the experiment, the simulated discharge is adapted to the experimentally investigated discharge by varying the gas temperature, the thermal electron desorption flux and the secondary electron emission coefficients in [11]. A good agreement is achieved using the parameter set with a gas temperature of $T_{gas} = 300$ K, a thermal electron desorption flux of $J_{des} = 10^{11}$ cm^{-2} s^{-1} and a secondary electron emission coefficient $\gamma_+ = 0.01$ for the first breakdown. This good agreement is exemplarily shown in figure 4(a), where the electrical quantities as the applied voltage, the gap voltage and the discharge current are plotted from the simulation and the experiment for the negative half cycle. Despite the good agreement, the discussion in [11] already showed that several parameter sets are appropriate to get a similar agreement with the experiment. The influence of such a discharge parameter variation is investigated in section 4.6.

Besides the electrical quantities in figure 4(a), the reduced electric field strength and the total ionization rate from the simulation are plotted in (b) and (c), repectively. Characteristic for this discharge is the first glow-like breakdown with the distortion of the externally applied electric field in (b) and the cathode-directed ionizing front in (c). The drop in gap voltage during the first breakdown is small, therefore a second breakdown occurs with a slightly distorted electric field. This second breakdown occurs without a cathode directed ionizing front, and shows an exponentially increasing ionization rate towards the anode, which is typical for Townsend-like breakdowns.
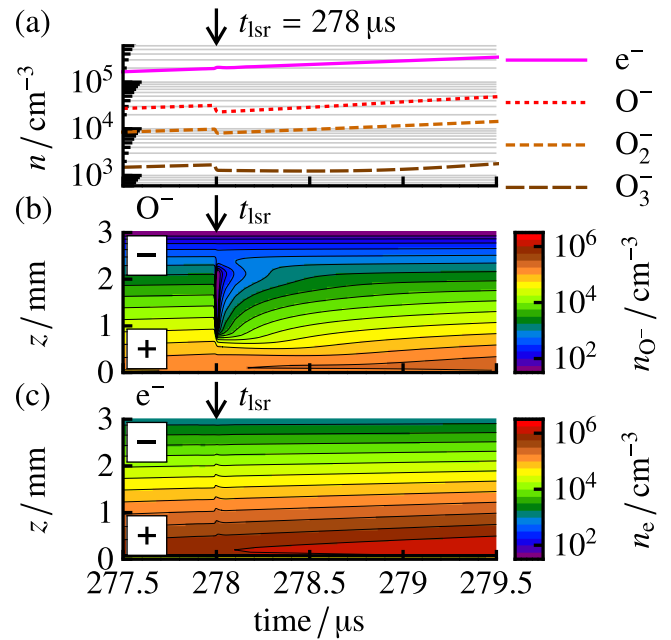
4.2. Laser photodetachment for adapted discharge

As mentioned, the discussion starts including the laser photodetachment in the adapted simulated discharge from [11]. The changes in electron and negative ion density by the laser photodetachment are presented for the time scale of the laser pulse in figure 5 using the box profile (4) with $s = 0.1$ mm and the maximal laser pulse energy of 100 mJ. The latter assures the detachment of almost all negative ions in the center of the laser beam. The chosen laser firing time of 278 μs is during the pre-phase of the first discharge current pulse in the negative half cycle, when the largest influence of the laser photodetachment on the discharge behavior was observed in the experiment. In figure 5(a), the spatially averaged densities of electrons and negative ions are plotted. During the laser pulse, the spatially averaged density of negative ions decreases, but not even half of the negative ions become detached. The spatio-temporally resolved O^- density in figure 5(b) reveals that the O^- ions are detached only in the central part of the gap, where the number density of laser photons is largest (compare figure 3). In this central part, the O^- density decreases by several orders of magnitude, but the larger negative ion density in front of the dielectrics remains nearly unchanged. Therefore, the spatially averaged O^- density in (a) decreases only slightly. After the laser pulse, the density of negative ions increases further because of electron attachment in the volume and the increasing electron density during the pre-phase of the discharge. In contrast to the negative ions, the spatially averaged electron density in (a) shows a very small peak during the laser pulse. The height of the peak is given by the negative ion density just before firing the laser, which is about one order of magnitude lower than the electron density. Hence, the spatially averaged electron density increases by less than ten percent during the laser pulse, which is
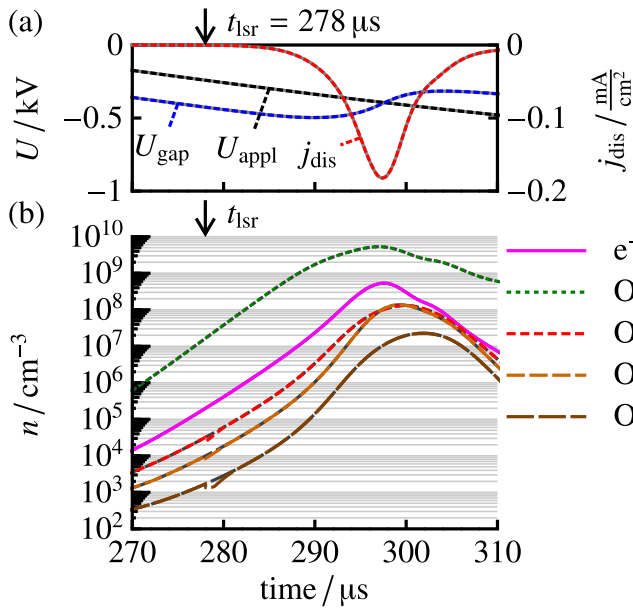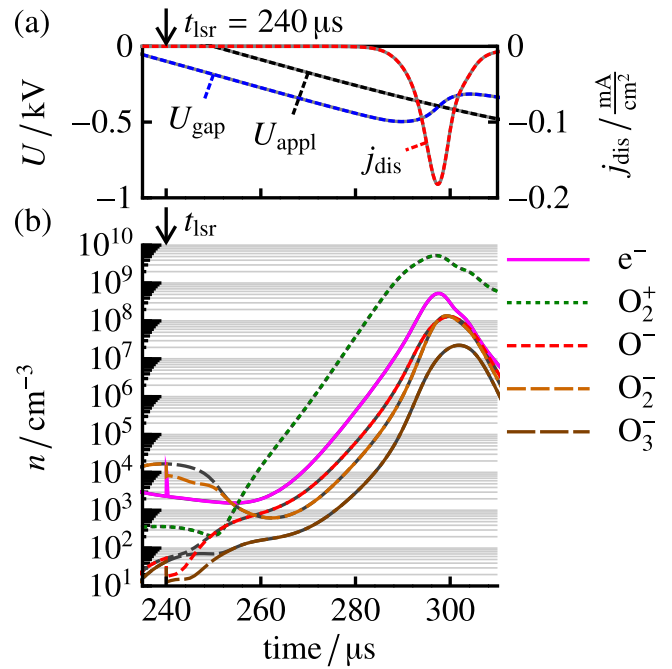
Figure 6. Influence of the laser photodetachment at $t_{lsr} = 278\,\mu s$ on the adapted discharge: (a) applied voltage, gap voltage, discharge current density and (b) spatially averaged densities of important species without (gray) and with laser photodetachment (colored) (box-shaped laser beam profile, $z = 1.5$ mm, $s = 0.1$ mm, $E_{lsr} = 100$ mJ).

Figure 7. Influence of the laser photodetachment at $t_{lsr} = 240\,\mu s$ on the adapted discharge: (a) applied voltage, gap voltage, discharge current density and (b) spatially averaged densities of important species without (gray) and with laser photodetachment (colored) (box-shaped laser beam profile, $z = 1.5$ mm, $s = 0.1$ mm, $E_{lsr} = 100$ mJ).

hard to see in logarithmic scale. The spatio-temporally resolved electron density in (c) increases only little during the laser pulse, but there is also an effect nearby the anode due to the drifting electrons from the center. Nonetheless, after this electron beam no long-lasting change in electron density is observed.

To analyze the effect of the laser photodetachment on the discharge, the time scale is extended in figure 6 to include the pre-phase and the breakdown of the discharge. Besides the spatially averaged electron, negative ion and O_2^+ densities in (b), the most important electrical quantities as the applied voltage, the gap voltage and the discharge current are presented in (a). In both plots, the discharge without laser photodetachment is represented by solid gray lines, whereas the laser-affected discharge is shown by dashed colored lines. It is easy to see that the electrical quantities of the discharge in (a) with and without laser photodetachment do not differ. Looking at the spatially averaged densities in (b), the peak in electron density during the laser photodetachment is too small to significantly increase the O_2^+ density, which would indicate an enhanced pre-ionization before the breakdown. Furthermore, the figure shows that the negative ion densities approach to the curves without laser photodetachment within some microseconds. This confirms that the perturbation in negative ion density by the laser photodetachment is only temporally.

As shown, the negative ion density at $278\,\mu s$ is too low to cause the laser photodetachment effect as in the experiment. However, there are times when the negative ion density is larger than the electron density, e.g. just after the change in gap voltage polarity. At this time, the O_2^- density exceeds the electron density because of the very effective attachment in

three particle collisions with the background gas

$$e^- + O_2 + He \rightarrow O_2^- + He \qquad (5)$$
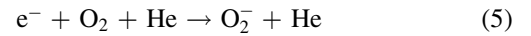
at low electric field (compare [11]). Since no laser photodetachment effect was observed in the experiment at this time, there must be another reason for the vanishing laser photodetachment effect. To point this out, the electrical quantities and the particle densities of the most important charged particles are shown in figure 7, but for a laser firing time of $t_{lsr} = 240\,\mu s$. In (b), it is visible that the larger O_2^- density during the laser photodetachment results in a large peak in electron density, but there is nearly no change in the O_2^+ density. The electric field at $t = 240\,\mu s$ is too low to induce ionization processes by the detached electrons. The detached electrons drift towards the anode without a significant influence on the ionization dynamics. As a consequence, both the discharge current density and gap voltage presented in (a) do not change.

In summary, these examples show that the negative ion density of the discharge using the common set of rate coefficients for electron attachment is not large enough to explain the laser photodetachment experiments. This is also the case when shifting the laser firing time to later times, since the negative ion density is always lower than the electron density during the pre-phase and breakdown of the discharge. Hence, additional processes producing larger negative ion density has to be considered in the simulation, or the used rate coefficients are not well quantified, in particular for the case of low electric fields in the pre-phase. Motivated by the experiment, two assumptions are made to achieve large negative ion densities in

Table 2. Readapted desorption flux and secondary electron emission coefficients for the conditions with larger attachment rates.

|	$J_{des} \times cm^2\,s$	γ_+
Attachment rates $\times$ 1	10^{11}	0.01
Attachment rates $\times$ 20	2×10^{11}	0.02
Attachment rates $\times$ 50	5×10^{11}	0.05
Attachment rates $\times$ 100	2×10^{12}	0.20

the simulation: (1) consideration of larger attachment rates in the volume, and (2) involving of secondary negative ion emission from the negatively charged dielectric. The laser photodetachment effect of both approaches is discussed in the following and compared to the experiment to allow conclusions about the actual source of negative ions.

4.3. Enhanced attachment in the volume

The previous discussion showed that the negative ion density in the simulation has to be clearly larger to get a laser photodetachment effect as observed in the experiment. Hence, the attachment rates might be underestimated or there might be missing attachment processes in the simulation. Therefore, in a first step, larger attachment rates are considered in the simulation. As it was already shown in [11], the increase of the attachment rates results in a wider discharge current pulse. Therefore, the flux J_{des} of thermally desorbed electrons from the cathode and the secondary electron emission coefficients $\gamma_+ = \gamma_{ph}$ were increased after assuming larger attachment rates. These changes are summarized in table 2 and have an influence on the laser photodetachment effect as well, which is investigated in section 4.6.

To point out the influence of larger attachment rates on the laser photodetachment effect, the spatially averaged densities of electrons and negative ions during the laser pulse are shown in figure 8(a) for the case of 100 times larger attachment rates. In contrast to the unmodified adapted simulation (compare figure 5), the negative ion densities exceed the electron density before the laser pulse. During the laser pulse, these large negative ion densities cause an increase in electron density by one order of magnitude. This peak in electron density falls off very rapidly, but remains afterwards on a level which is larger than before the laser photodetachment. This behavior can be understood by looking at the spatio-temporally resolved O^- and electron density in figure 8(b) and (c), respectively. The O^- density behaves as in figure 5, but the spatially resolved electron density in (c) shows an electron beam initiated by the laser pulse. Because of the large electron drift velocity, these beam electrons are gone within less than 0.2 μs, which explains the sharp peak in electron density during the laser pulse in (a).

To clarify the long-lasting increase of the electron density after the laser photodetachment and to see the influence on the discharge breakdown, the electrical quantities and the spatially averaged densities of the most important species are presented in figure 9 for different laser firing times. As before,
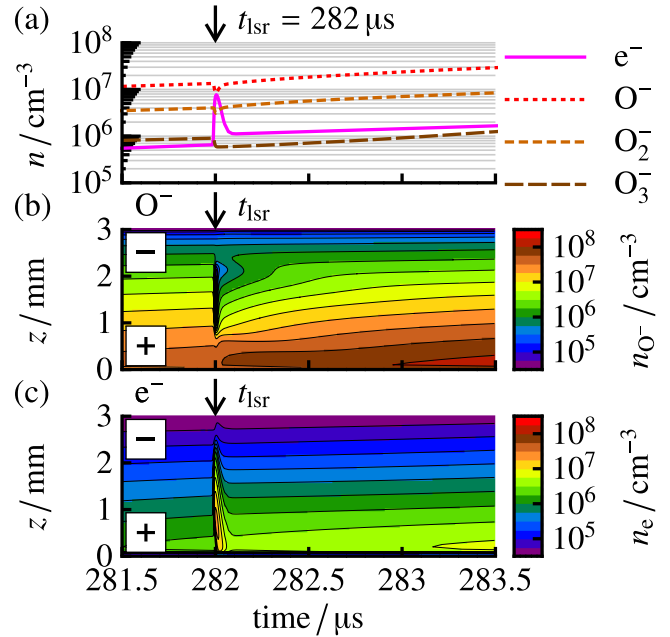
Figure 8. Change in negative charges by laser photodetachment with 100 times larger attachment rates: (a) spatially averaged densities and spatio-temporally resolved density of (b) O^- ions and (c) electrons (box-shaped laser beam profile, $z_{lsr} = 1.5$ mm, $s = 0.1$ mm, $t_{lsr} = 282$ μs, $E_{lsr} = 100$ mJ).

the unaffected simulated discharge (gray) is shown in comparison to the laser-affected ones (colored). For all laser firing times, the electron density is increased during the laser pulse by about one order of magnitude. The decreases in O^- and O_2^- densities are hard to see, because of the large time scale and the strongly enhanced electron attachment in this simulation. In contrast, the O_3^- density remains longer on the level caused by the photodetachment, because it is mainly formed by three particle collisions of O^- with O_2 and the background gas. Besides, the detached beam-like electrons cause immediately an increase in helium metastables density, because the helium metastables are excited by electron impact excitation

$$e + He \rightarrow He^m + e. \tag{6}$$
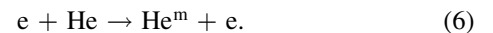
Afterwards, these metastables produce additional O_2^+ ions by Penning-ionization

$$He^m + O_2 \rightarrow O_2^+ + He \tag{7}$$

with a delay of several microseconds. The increased number of O_2^+ ions results in a larger secondary electron emission and larger electron density compared with the unaffected discharge as well. This explains the long-lasting increase in electron density as seen in figure 8.

Looking at the laser induced changes in discharge current and gap voltage in figure 9, the laser firing at $t_{lsr} = 270$ μs in (a) has no effect, whereas the laser firing just before the breakdown at $t_{lsr} = 282$ μs in (b) and during the breakdown at $t_{lsr} = 294$ μs in (c) change the electrical characteristics. For $t_{lsr} = 270$ μs, the laser firing is too early and the perturbation relaxes before the discharge breakdown. In the second case at $t_{lsr} = 282$ μs, the laser firing time is close enough to the
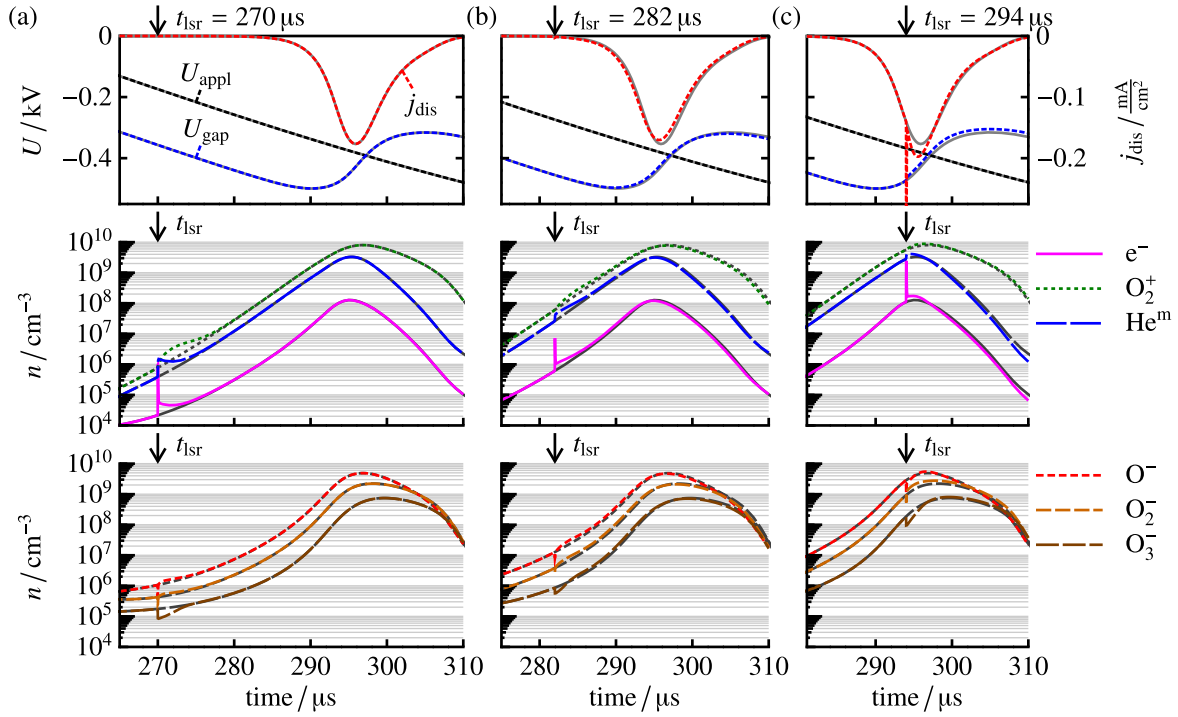
Figure 9. Influence of the laser photodetachment on the discharge with 100 times larger attachment rates: applied voltage, gap voltage, discharge current density (top) and spatially averaged densities of important species (center, bottom) without (gray) and with laser photodetachment (colored) at (a) $t_{lsr} = 270\,\mu s$, (b) $t_{lsr} = 282\,\mu s$, (c) and $t_{lsr} = 294\,\mu s$ (box-shaped laser beam profile, $z = 1.5$ mm, $s = 0.1$ mm, $E_{lsr} = 100$ mJ).

breakdown. The larger pre-ionization results in a slight decrease in breakdown voltage (hard to see in figure 9(b)) and the discharge current pulse shifts to earlier times, which equals the observed laser photodetachment effect in the experiment. In the third case for a laser firing time during the discharge current pulse at $t_{lsr} = 294\,\mu s$, the laser photodetachment induces both an additional short current pulse at the laser firing time and an enhancement of the discharge current pulse. This larger discharge current causes a significant change in gap voltage after the breakdown, too.

To compare the laser photodetachment effect with the experiment quantitatively, the temporal shift of the discharge current pulse minimum

$$\Delta t = t_{min}^{without\ lsr} - t_{min}^{with\ lsr}. \qquad (8)$$

(t_{min}: time of minimal discharge current density) and the change in transported charge per area

$$\Delta\sigma = \int_{260\,\mu s}^{330\,\mu s} j_{dis}^{with\ lsr}(t)dt - \int_{260\,\mu s}^{330\,\mu s} j_{dis}^{without\ lsr}(t)dt, \qquad (9)$$

which is the difference in surface charge density after the first discharge current pulse

$$\Delta\sigma = \sigma^{with\ lsr}(330\,\mu s) - \sigma^{without\ lsr}(330\,\mu s), \qquad (10)$$

are determined. Due to the negative discharge current density, $\Delta\sigma$ becomes positive when less charges are transported during the laser affected discharge. Both Δt and $\Delta\sigma$ are plotted depending on the laser firing time t_{lsr} for 20, 50 and 100 times larger attachment rates in the simulation in figures 10(b) and (c). Besides, the experimental values from
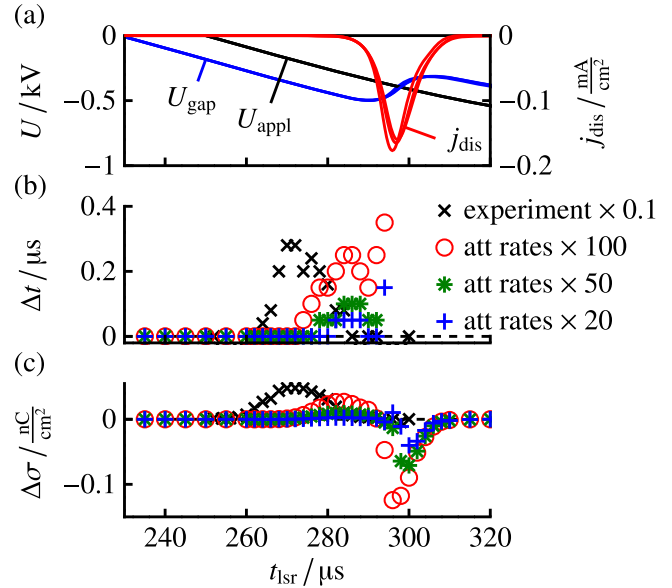

Figure 10. Influence of the laser photodetachment depending on the laser firing time assuming larger attachment rates: (a) applied voltage, gap voltage and discharge current density of the unaffected discharges. (b) Temporal shift of the discharge current pulse minimum and (c) change in transported charge per area (box-shaped laser beam profile, $z_{lsr} = 1.5$ mm, $s = 0.1$ mm, $E_{lsr} = 100$ mJ) in comparison to the scaled experimental values.

[10] are added and the electrical quantities of the unaffected simulated discharge are shown in figure 10(a) for comparison. The curves of the discharge current density and the gap voltage are slightly different because of the influence of the

enhanced attachment on the discharge and the resulting different parameter listed in table 2. Looking at the laser photodetachment effect in (b) and (c), first of all, there is no effect in the early pre-phase ($t_{lsr} < 260\ \mu$s) for all conditions because the perturbation given by the laser photodetachment relaxes within several microseconds. The simulated laser photodetachment effect starts at $t_{lsr} = 270\ \mu$s and reaches its maximum at about $284\ \mu$s for 100 times larger attachment rates. At these times the perturbation is close enough to the discharge breakdown to have an effect on it. The height of the maximum depends on the used factor for the attachment rates, which is the reasonable behavior because of the larger ratio of the negative ion density to the electron density for larger attachment rates. After the maximum, the time shift Δt in (b) decreases until $290\ \mu$s (for 100 times larger attachment rates) and increases again after $290\ \mu$s. For the lower attachment rates, this behavior is hard to see, because the time shift Δt undercuts the saving times of the simulation. This problem does not occur for $\Delta\sigma$ in (c), where even small differences are visible. Until the maximum at about $t_{lsr} = 284\ \mu$s, the curve of $\Delta\sigma$ equals the curve of Δt, but after the maximum it decreases and changes its polarity at about $t_{lsr} = 295\ \mu$s. For times later than $t_{lsr} = 295\ \mu$s, $\Delta\sigma$ is negative, which means that the laser photodetachment causes a larger discharge current and more transported charges during the discharge current pulse. The absolute value of $\Delta\sigma$ for these times is even larger in comparison to the value during the pre-phase. This was never observed in the experiments, where the largest effect was observed when firing in the pre-phase of the discharge. Hence, the negative ion density during the discharge current pulse has to be clearly lower, and this is not fulfilled by the assumption of 100 times larger attachment rates. If there are actually missing attachment processes in the simulation, then they should have their maximum at low electric fields to enhance the formation of negative ions in the pre-phase, but not during the discharge current pulse. Besides the qualitative discrepancy, there is also a quantitative difference between the simulation and the experiment concerning the maximum during the pre-phase. In comparison to the experiment, the maximum is too late and by at least a factor of ten too small. That means, although the O^- density is more than 10 times the electron density (compare figure 9), this difference is not large enough to reproduce the laser photodetachment effect of the experiment quantitatively. Hence, either the attachment rate has to be much larger or the influence of the detached electrons on the simulated discharge is too weak.

Before considering alternative processes for an enhanced negative ion production, the dependence of the laser photodetachment effect, quantified by the change in transported charge per area $\Delta\sigma$, on the laser pulse energy is presented in figure 11 for the different laser beam profiles. For comparison, the experimentally measured curve and the photodetachment ratio

$$\frac{\Delta n_e}{n_{O^-}} = 1 - \exp\left(-\frac{E_{lsr}}{E_{O^-}}\right) \text{ with } E_{O^-} = \frac{A_{lsr}}{\sigma_{O^-}} \frac{hc_0}{\lambda_{lsr}} \qquad (11)$$
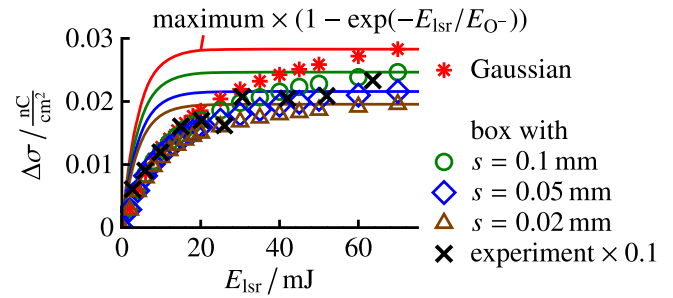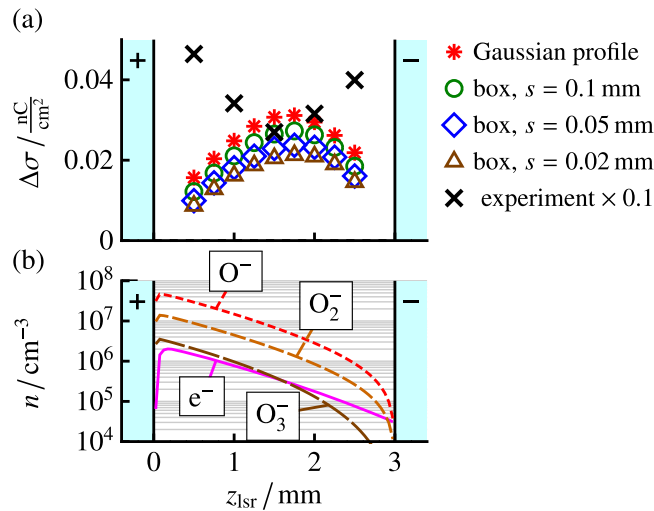

Figure 11. Change in transported charge per area depending on the laser pulse energy for different laser beam profiles assuming 100 times larger attachment rates ($z_{lsr} = 1.5$ mm, $t_{lsr} = 282\ \mu$s). Additionally, the scaled experimental values and the analytical saturation curves for O^- are plotted.

from the zero-dimensional analytical model in [10] are shown ($A_{lsr} = 6$ mm^2, Planck's constant h, speed of light c_0, $\sigma_{O^-} = 6.4 \times 10^{-18}$ cm^2, $\lambda_{lsr} = 532$ nm). For the analytical curve, only the dominant negative ion O^- is considered. The curves resulting from the simulation show a steep increase for low laser pulse energies and a flattening after 20 mJ. A saturation value is not reached for $E_{lsr} \leqslant 70$ mJ, but the curves become flatter for sharper laser beam profiles ($s \to 0$). Hence, the further increase of the simulated laser photodetachment effect above 20 mJ is caused by the wings of the laser beam profile, which allow further laser photodetachment nearby the dielectrics even when saturation is already reached in the central part of the laser beam. Furthermore, the agreement of the curves resulting from the simulation with the experimental one is much better than the agreement with the analytical model. This means that the laser photodetachment of O^- in combination with a slightly blurred laser beam profile, e.g. with $s = 0.02$ mm, can already explain the laser pulse energy dependence of the experiment. Therefore, the dependency obtained by the simulation dissolves the contradiction between the comparison of the measured laser pulse energy dependence with the analytical model in [10]. The statement that O^- is the dominating ion species remains valid.

To allow conclusions about the spatial distribution of the negative ions, the axial profile of the laser photodetachment effect was measured by determining the change in transported charge per area $\Delta\sigma$ for different axial positions z_{lsr} of the laser beam. Such a measurement is compared to the results from the simulation in figure 12(a) for the different laser beam profiles. For all laser beam profiles, the curves resulting from the simulation are very similar to each other. They have their maximum nearby the center of the gap and they decrease towards both dielectrics. The absolute value of the photodetachment effect increases for the wider profiles, which is reasonable because of the larger photodetachment rate in the wings of the wider profiles. In comparison to the experiment, the values from the simulation are smaller and their dependence on the axial position is vertically inverted. The experimental curve has its minimum in the center.

To understand the shapes of the axial profiles obtained from the simulation, the density profiles of the negative

Figure 12. Axial profiles of (a) the laser-affected change in transported charge per area for various laser beam profiles assuming 100 times larger attachment rates ($E_{lsr} = 100$ mJ, $t_{lsr} = 282$ μs) in comparison to the scaled experimental values and (b) the electron and negative ion densities of the unaffected discharge.

species are shown in figure 12(b) for comparison. For the strength of the laser photodetachment effect, it is important how many electrons become detached and where they become detached. The electrons which are detached in front of the cathode have a longer way to the anode than the detached electrons in front of the anode, therefore they can induce further ionization processes on their way to the anode and the laser photodetachment effect becomes larger. In contrast, the negative ion density increases towards the anode, hence, more electrons are detached there. Since the multiplication factor of electrons (effective Townsend's ionization coefficient α_{eff}) is the same as the increase of the electron density and the O^- ion density towards the anode (see figure 12(b)), both aspects together should end in a nearly constant profile. Nonetheless, deviations from such a constant profile are clearly visible. The decrease in front of the cathode might result from the lower ratio of negative ions to the electrons there and the decrease towards anode might be caused by the slightly increasing electric field towards the cathode at this late time of the pre-phase.
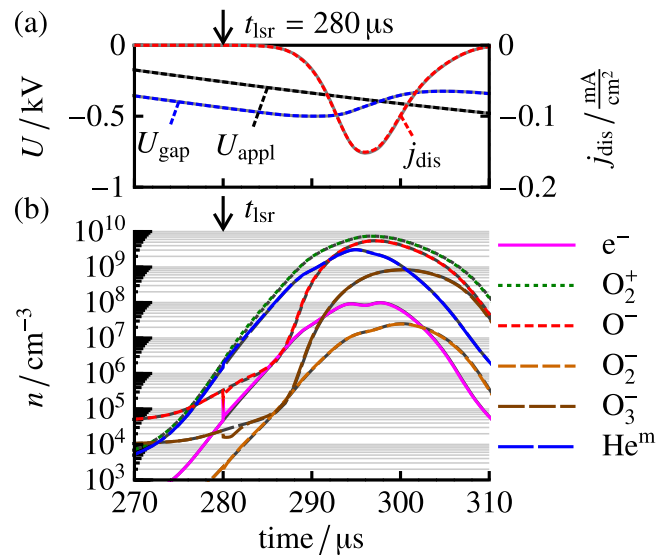
4.4. Enhanced attachment at low electric fields

The assumption of 100 times larger attachment rates in the simulation can reproduce the laser photodetachment effect in the pre-phase quantitatively, but the larger negative ion density during the discharge current pulse causes a large effect at these times, too. This was never observed in the experiment, hence, the attachment might be larger during the pre-phase only. This would require an additional attachment process with a maximum at low electric field strength. To analyze such an approach, a dissociative three-particle attachment process

$$e^- + O_2 + He \rightarrow O^- + O + He \qquad (12)$$
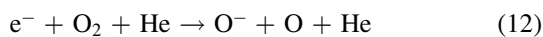
is introduced with a maximal rate coefficient of 10^{-27} cm^6 s^{-1} at 9 Td. The corresponding two-particle collision rate coefficient is
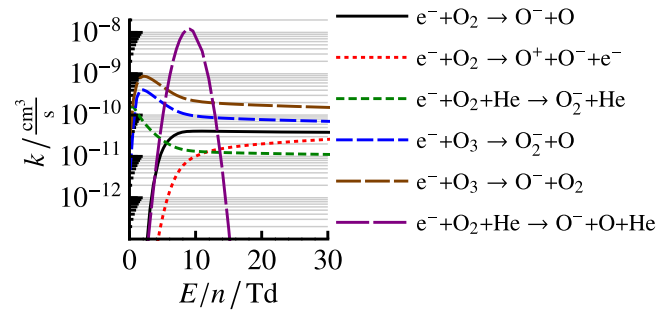

Figure 13. Rate coefficients for attachment processes depending on the reduced electric field strength in comparison to the artificial rate coefficient for dissociative three-particle attachment.

Figure 14. Influence of the laser photodetachment on the discharge with the assumption of an additional attachment process at low electric field strengths: (a) applied voltage, gap voltage, discharge current density and (b) spatially averaged densities of important species without (gray) and with laser photodetachment (colored) at $t_{lsr} = 280$ μs (box-shaped laser beam profile, $z = 1.5$ mm, $s = 0.1$ mm, $E_{lsr} = 100$ mJ).

compared to the most important attachment rates in figure 13. The threshold value is similar to the two-particle collision attachment process, but the chosen maximum exceeds the other processes by two orders of magnitude to ensure a similar ratio of the negative ion density to the electron density as in the case of 100 times larger attachment rates. For reduced electric field strengths larger than 15 Td, as it is typical during the breakdown, the rate coefficient of the artificial process is lower than the common ones. This should limit the overall attachment during the discharge current pulse.

The effect on the electrical quantities of the discharge and the particle densities is presented in figure 14 when firing the laser during the pre-phase at 280 μs. Figure (b) shows that the O^- density exceeds the electron density in the early pre-phase as it is intended by the artificial attachment process. Since the O^- density is only one order of magnitude larger than the electron density at 280 μs, the change in discharge current and gap voltage is very small. Hence, to reproduce the
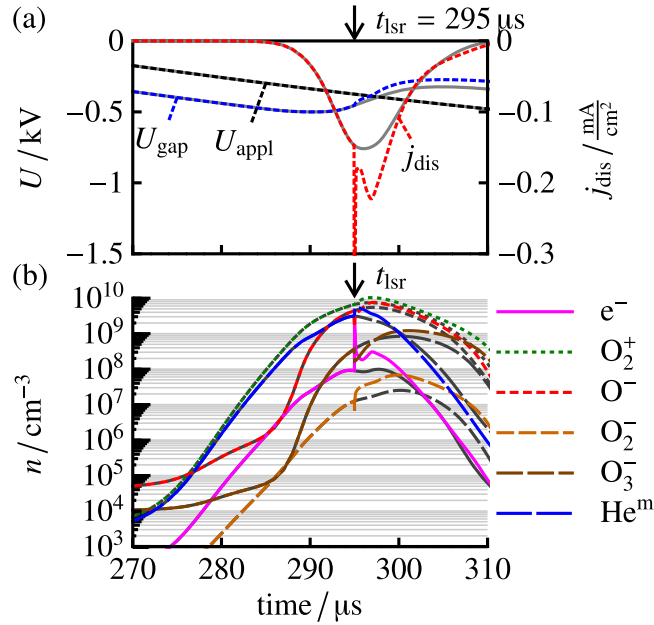
Figure 15. Influence of the laser photodetachment on the discharge with the assumption of an additional attachment process at low electric field strengths: (a) applied voltage, gap voltage, discharge current density and (b) spatially averaged densities of important species without (gray) and with laser photodetachment (colored) at $t_{lsr} = 295\ \mu s$ (box-shaped laser beam profile, $z = 1.5$ mm, $s = 0.1$ mm, $E_{lsr} = 100$ mJ).
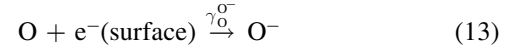
measured laser photodetachment effect quantitatively, an even larger rate coefficient would be necessary. Furthermore, although the rate coefficient decreases drastically after its maximum at 9 Td, the formation of negative ions during the discharge current pulse is large as well. On the one hand, the attachment in front of the cathode is actually lower in comparison to the simulation with 100 times larger attachment rates, because of the larger field there. But on the other hand, the lower electric field strength in front of the anode is comparable to the electric field strength in the pre-phase (compare figure 4), and therefore the electron attachment in front of the anode is as well comparable to the electron attachment in the pre-phase. Hence, it is necessary to look at a possible laser photodetachment effect when firing the laser during the discharge current pulse. This situation is plotted in figure 15 for a laser firing time of 295 μs. As visible, the laser photodetachment releases a large amount of electrons and a large additional current as well as a larger drop in gap voltage are induced. This effect is much larger than the effect in the pre-phase, which is again a large contradiction to the observations from the experiment. Hence, the assumption of a larger attachment process at low electric field strength to increase the number density of negative ions during the pre-phase causes always larger attachment rates during the discharge current pulse and afterglow in the regions with low electric fields as well. This is related to a larger laser photodetachment effect during the discharge current pulse, too, but this was not observed in the experiment. In conclusion, an additional attachment process in the volume with a rate coefficient depending on the electric field cannot reproduce the laser photodetachment experiment.

Other processes have to be considered, which are able to enhance the negative ion density during the pre-phase, but not during the discharge current pulse.
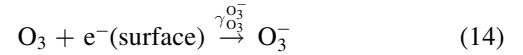
4.5. Negative ion production at the surface

Besides additional attachment processes in the volume, the formation of negative ions at the dielectric surfaces might cause larger negative ion densities. Usually, such processes of negative ions on a surface are not considered in simulations, but mass spectrometry measurements at low pressure radio-frequency discharges in oxygen indicate that they are an important source of negative ions [21, 22]. Furthermore, the formation of negative hydrogen ions on surfaces is already used in ion beam sources for fusion devices [23, 24].

To have an influence on the negative ion density in the volume of barrier discharges, the surface process has to take place at the cathodic dielectric, because solely the negative ions formed there are able to drift through the gap. Furthermore, the surface of the cathodic dielectric is negatively charged by electrons from the previous breakdown. These surface electrons are weakly bound in the solid or even trapped in an electron surface layer in front of the dielectric [25, 26]. Their binding energy is in the order of 1 eV [27–29]. This is in the same range as the electron affinity of oxygen atoms (1.46 eV) and ozone molecules (2.10 eV). Hence, resonant charge transfers

$$O + e^-(\text{surface}) \xrightarrow{\gamma_O^{O^-}} O^- \quad (13)$$

and

$$O_3 + e^-(\text{surface}) \xrightarrow{\gamma_{O_3}^{O_3^-}} O_3^- \quad (14)$$

of surface electrons to the oxygen atoms or ozone molecules are possible, since the electron affinity of O and O_3 can compensate the binding energy of electrons on the surface. In contrast to O^- and O_3^-, a resonant charge transfer is not considered for O_2^-, because the electron affinity of O_2 (0.45 eV) is probably lower than the binding energy of the surface electrons. Furthermore, the experiments with the fundamental wavelength of the Nd:YAG laser exclude O_2^- as the main negative ion species. The coefficients $\gamma_O^{O^-}$ and $\gamma_{O_3}^{O_3^-}$ in (13) and (14) describe the probability to form a negative ion per impinging oxygen atom or ozone molecule, respectively. They are varied between 10^{-6} and 0.01 in the simulation. The value of 0.01 is the upper limit when having a reflexion coefficient of $r = 0.99$ as used for the adapted simulation. In this case every lost oxygen atom and ozone molecule transforms into a negative ion at the surface.

The reaction (13) is implemented in the simulation by setting the flux of O^- ions from the surface to

$$J_{O^-}^{\text{from surface}} = -\gamma_O^{O^-} J_O^{\text{to surface}}, \quad (15)$$

wherein

$$J_O^{\text{to surface}} = \mp \frac{1}{4} v_{th} n_O - \frac{1}{2} D_O \frac{d\,n_O}{d\,z} \quad (16)$$

10

is the flux to the surface [30], v_{th} the thermal velocity, n_O the density, and D_O the diffusion coefficient of oxygen atoms. The $-$ sign is valid for $z = 0$, and the $+$ sign for $z = 3$ mm. The equations for O_3^- ions are alike. Furthermore, it is worth to notice that the generated O^- and O_3^- ions have a finite probability to go back to the surface due to their thermal movement. The negative ions reaching the surface are loosing their electron to the surface and form an oxygen atom or ozone molecule since the reflection of negative particles at the surface is not considered in the simulation. Including the reflection of negative ions at the surfaces would increase the number of negative ions reaching the volume when they become created at the cathodic surface. However, since the coefficients $\gamma_O^{O^-}$ and $\gamma_{O_3}^{O_3^-}$ are anyhow unknown, the discussion is limited to the case where negative ions are not reflected from the surface.

For low values of $\gamma_O^{O^-}$ and $\gamma_{O_3}^{O_3^-}$, the discharge does not change, but for $\gamma_O^{O^-} \geqslant 0.001$ a significant flux of O^- ions is present and the subsequent detachment in the volume contributes significantly to the electron production in the pre-phase of the discharge. In particular, this process exceeds the production of electrons by thermal desorption at the surface in the pre-phase of the simulated discharge. Hence, to avoid changes in the discharge characteristics, only low values of $\gamma_O^{O^-}$ are discussed in the following.

The effect of the laser photodetachment on the electron and negative ion densities during the pre-phase, including the production of negative ions at the negatively charged dielectric with $\gamma_O^{O^-} = \gamma_{O_3}^{O_3^-} = 10^{-4}$, is shown in figure 16(a). In comparison to the simulated discharge without the formation of negative ions at the surface (compare figure 5), the spatially averaged O^- and O_3^- densities exceed the electron density before the laser pulse. As for the simulations with the enhanced attachment (compare figure 8), this larger negative ion density causes a steep increase in electron density during the laser pulse and a significant larger electron density after some microseconds. Looking at the spatial distribution of the O^- ions in figure 16(b), their density before the laser pulse is constant along the gap and no longer exponentially increasing towards the anode. As for the previous conditions, the laser pulse tears a hole in the spatially and temporally constant O^- density. This hole evolves with the O^- drift velocity towards the anode, and it becomes refilled by the O^- ions which are formed at the cathodic dielectric. The spatio-temporally resolved electron density is presented in figure 16(c). An electron beam develops at the time of the laser pulse. Although the laser intensity in front of the dielectrics is low, the beam electrons even start at the cathodic dielectric because of the large O^- density there. The beam is gone within 0.2 μs when touching the anodic dielectric, but the electron density remains significantly larger after the laser pulse in comparison to the time before the laser pulse. Hence, for this case, a long-lasting effect is visible.

To investigate the influence on the discharge as in the previous sections, the time-line is extended in figure 17 for three different laser firing times and the electrical quantities are shown for comparison. As before, the colored lines mark
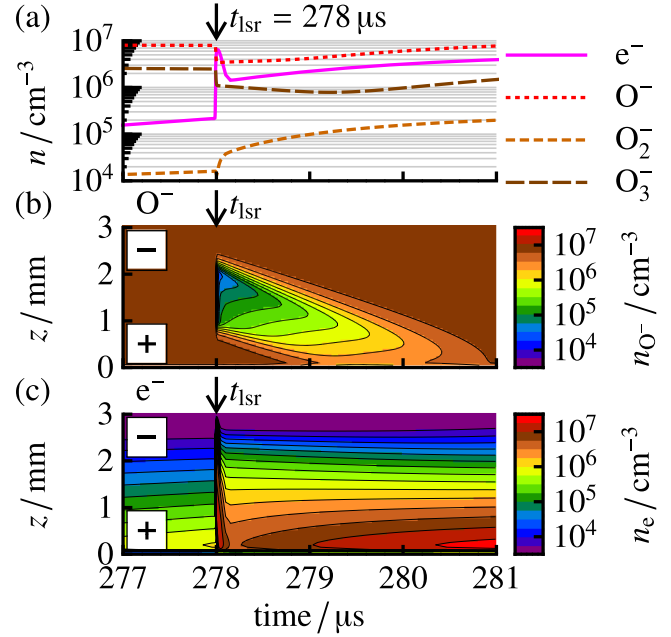

Figure 16. Change in negative charges by laser photodetachment with the additional production of negative ions at the negatively charged dielectric ($\gamma_O^{O^-} = \gamma_{O_3}^{O_3^-} = 10^{-4}$): (a) spatially averaged densities and spatio-temporally resolved density of (b) O^- ions and (c) electrons (box-shaped laser beam profile, $z_{lsr} = 1.5$ mm, $s = 0.1$ mm, $t_{lsr} = 278$ μs, $E_{lsr} = 100$ mJ).

the laser affected discharge, and the gray lines the unaffected discharge. For a laser firing time of $t_{lsr} = 264$ μs in (a), the increase in electron density causes an immediate large increase in helium metastables and a delayed increase in O_2^+ ions by the subsequent Penning ionization. However, this enormous change in particle densities has no influence on the discharge current pulse, because of the low densities and the relaxation of the perturbation to the unaffected simulation within 15 μs. In contrast, firing the laser at $t_{lsr} = 278$ μs as shown in (b), the perturbation occurs during the crucial part of the pre-phase and the discharge ignites at a lower gap voltage and the discharge current pulse is shifted to earlier times as in the experiment. In figure 17(c), the laser firing time is shifted further to $t_{lsr} = 290$ μs. At this time, the discharge breakdown has already started before the laser photodetachment takes place. No significant influence on the discharge can be observed, since the electron density is already one order of magnitude larger than the negative ion density. Hence, the production of negative ions at the negatively charged surface accounts only in the pre-phase of the discharge, when the electron density is lower than the density of negative ions produced at the surface.

The behavior of the temporal shift of the discharge current pulse minimum Δt and the change in transported charge per area $\Delta \sigma$ are plotted for different laser firing times and different reaction probabilities $\gamma_O^{O^-}$ and $\gamma_{O_3}^{O_3^-}$ of the negative ion production at the negatively charged dielectric in figures 18(b) and (c). The electrical quantities of the unaffected discharge are
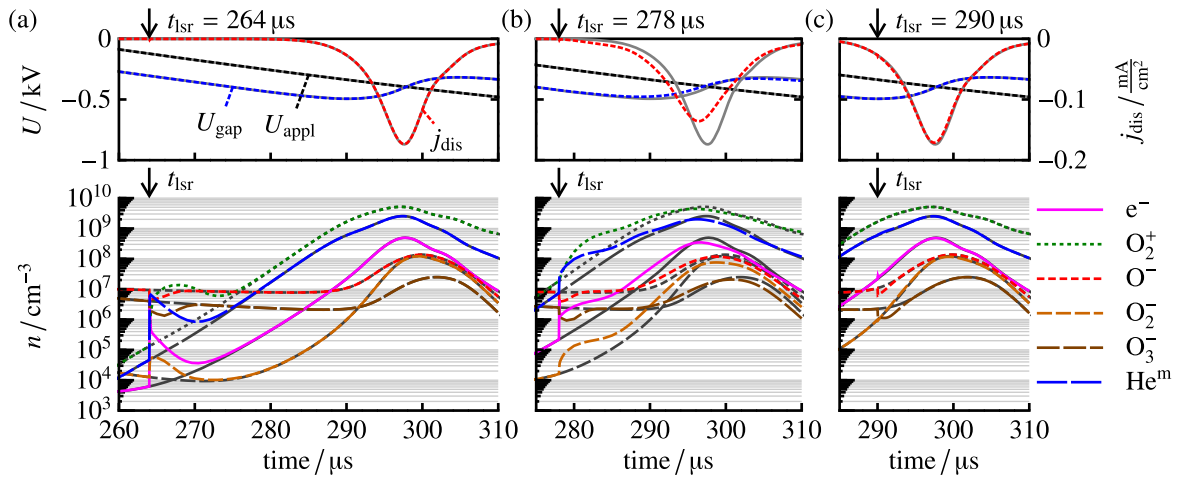
Figure 17. Influence of the laser photodetachment on the discharge with negative ion formation at the cathodic dielectric ($\gamma_{O}^{O^-} = \gamma_{O_3}^{O_3^-} = 10^{-4}$): applied voltage, gap voltage, discharge current density (top) and spatially averaged densities of important species (bottom) without (gray) and with laser photodetachment (colored) at (a) $t_{lsr} = 264\,\mu s$, (b) $t_{lsr} = 278\,\mu s$, (c) and $t_{lsr} = 290\,\mu s$ (box-shaped laser beam profile, $z = 1.5$ mm, $s = 0.1$ mm, $E_{lsr} = 100$ mJ).
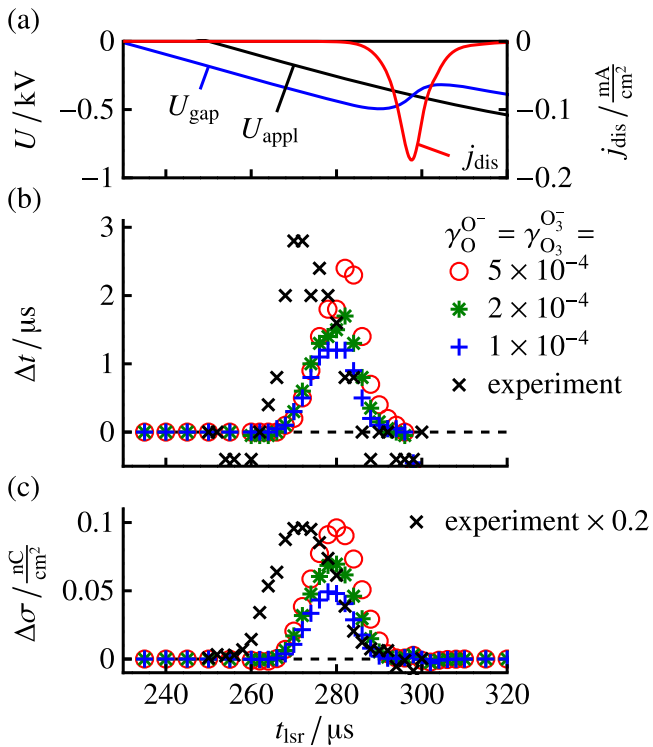

Figure 18. Influence of the laser photodetachment depending on the laser firing time assuming negative ion formation at the cathodic dielectric: (a) applied voltage, gap voltage and discharge current density of the unaffected discharge. (b) Temporal shift of the discharge current pulse minimum and (c) change in transported charge per area (box-shaped laser beam profile, $z_{lsr} = 1.5$ mm, $s = 0.1$ mm, $E_{lsr} = 100$ mJ) in comparison to the scaled experimental values.

shown for comparison in (a). At times before $260\,\mu s$, the discharge is not affected by the laser photodetachment, as well as for times later than $290\,\mu s$. For the early times, the perturbation given by the laser photodetachment relaxes before the discharge breaks down and for the later times, the electron

density exceeds the negative ion density. Only between 260 and $290\,\mu s$, a strong effect on the discharge is observable with a maximum in between these two values. Hence, all curves reflect the qualitative behavior obtained in the experiment, and the laser photodetachment effect increases as expected with increasing formation of negative ions at the dielectric. Quantitatively, the limits and the maxima are at earlier times in the experiment. The absolute value of Δt agrees best for $\gamma_{O}^{O^-} = 5 \times 10^{-4}$, but $\Delta\sigma$ is still about five times larger in the experiment. The value of $\gamma_{O}^{O^-} = 5 \times 10^{-4}$ in combination with the reflexion coefficient of $r = 0.99$ for oxygen atoms means that every twentieth lost oxygen atom becomes a negative ion at the surface, which is a reasonable value for such a process.

The dependence of the laser photodetachment effect on the laser pulse energy is illustrated by the change in transported charge per area $\Delta\sigma$ in figure 19. All curves increase with increasing laser pulse energy because of the larger amount of detached electrons at larger laser pulse energies. Saturation occurs only for small smoothing parameter s. For the sharp box profile with $s = 0.02$ mm, the curve is even in good agreement with the 0D analytical model in equation (11). The broader laser profiles still increase at their wings for larger laser pulse energies which causes a remarkable increase in the laser photodetachment effect. In contrast to the curves for the enhanced attachment in figure 11, the increase of the laser photodetachment is steeper and the saturation is less pronounced. The reason is the constant negative ion density across the gap, which allows a strong increase of the laser photodetachment in the wings of the laser beam profile.

Axial profiles of the laser photodetachment effect obtained from simulations with different laser profiles are presented in figure 20(a) by plotting the change in transported charge per area $\Delta\sigma$ over the axial laser position. For all laser beam profiles, $\Delta\sigma$ increases towards the cathode. As known, the electrons detached nearby the cathode have a longer way
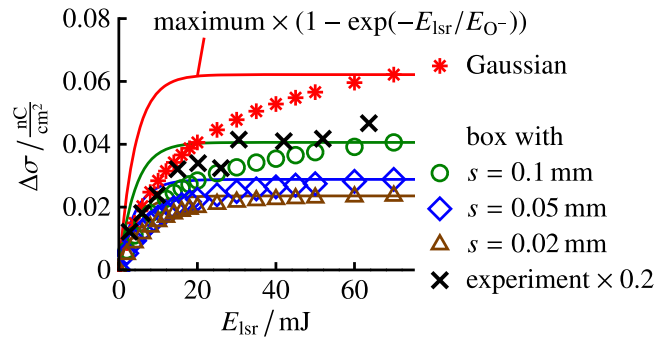
Figure 19. Change in transported charge per area depending on the laser pulse energy for different laser beam profiles assuming negative ion formation at the cathodic dielectric ($\gamma_O^{O^-} = \gamma_{O_3}^{O_3^-} = 10^{-4}$, $z_{lsr} = 1.5$ mm, $t_{lsr} = 278$ μs). Additionally, the scaled experimental values and the analytical saturation curves for O^- are plotted.
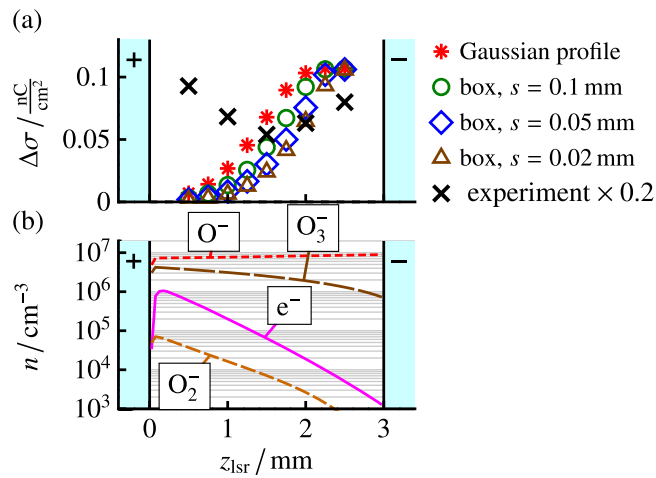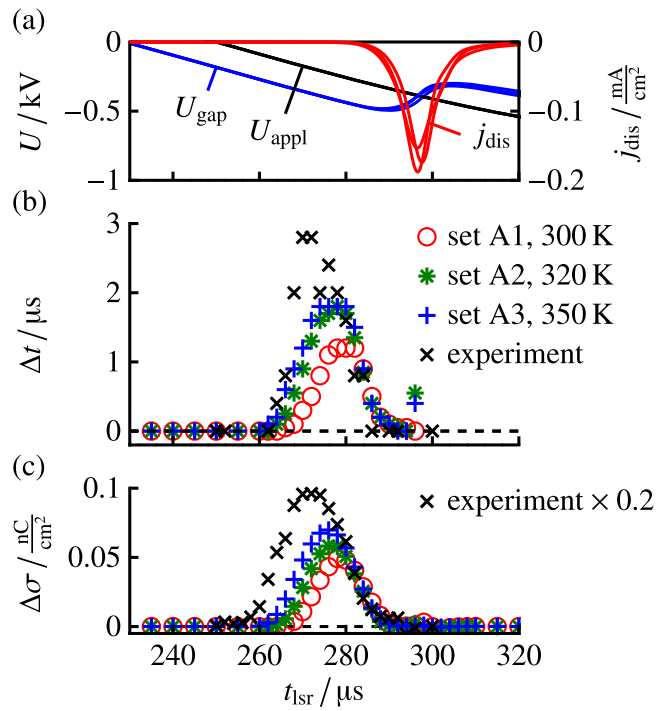

Figure 20. Axial profiles of (a) the laser-affected change in transported charge per area for various laser beam profiles assuming negative ion formation at the cathodic dielectric ($\gamma_O^{O^-} = \gamma_{O_3}^{O_3^-} = 10^{-4}$, $E_{lsr} = 100$ mJ, $t_{lsr} = 278$ μs) in comparison to the scaled experimental values and (b) the electron and negative ion densities of the unaffected discharge.

to the anode and induce a larger electron avalanche than the electrons starting nearby the anode. Hence, a released electron nearby the cathode has a larger influence on the discharge behavior than a released electron nearby the anode. Since the negative ion density is constant across the gap when assuming the negative ion production at the negatively charged dielectric (see figure 20(b)), the laser photodetachment effect increases towards the cathode as well. Comparing the curves for $\Delta\sigma$ in (a) from different laser profiles, the spatially broader profiles have a broader maximum in front of the cathode, too. The reason is again the larger influence of electrons detached nearby the cathode and the ability of the broader profiles to release these electrons. Despite the behavior obtained from the simulation is reasonable, there is no good agreement with the experimentally determined axial profile. The large values measured in front of the anode cannot be reproduced by the simulation with the assumption of a constant negative ion formation at the cathodic dielectric. Nonetheless, the good agreement concerning the temporal

behavior of the laser photodetachment effect supports the formation of negative ions at the surface as a realistic elementary process. The discrepancy of the axial profiles might result from the assumption of a temporally constant formation rate, given by the constant value of $\gamma_O^{O^-}$. Actually, the formation of negative ions by the resonant charge transfer of surface electrons and further electron emission processes, e.g. thermal desorption, reduce the number of surface electrons having the adequate energy level over time. Hence, the formation probability $\gamma_O^{O^-}$ should decrease in time. Such a decrease in the formation rate of negative ions at the surface would propagate across the gap, and it results in an increasing negative ion density towards the anode. This increase might compensate the effect that the detached electrons nearby the cathode have a larger influence on the discharge development, hence, an approximately constant profile of the laser photodetachment effect as in the experiment might appear. However, such a simulation needs a description of the energy levels at the surface to calculate a time-dependent negative ion formation probability $\gamma_O^{O^-}$, which is beyond the scope of this paper. Furthermore, the profile of the laser photodetachment effect was measured for one discharge condition only, so it is recommended to repeat this measurement for different discharge parameter (oxygen admixture, applied voltage) as was done for the laser firing time and the laser pulse energy variation.

4.6. Variation of adapted discharge parameter

The previous discussions showed that the ratio of the negative ion to the electron density is a crucial parameter for the strength of the laser photodetachment effect. During the prephase of the discharge, when the laser photodetachment effect is largest, the thermal desorption flux and the secondary electron emission coefficients have strong influence on the electron density. A comparison in [11] pointed out that different parameter sets of gas temperature T_{gas}, thermal electron desorption flux J_{des} and secondary electron emission coefficient γ_+ ($= \gamma_{ph}$) are able to reproduce the measured discharge current and voltage drop during the breakdown. Therefore, it is necessary to check how the laser photodetachment effect depends on the used parameter set in the simulation. Such a comparison is presented in figure 21 for the first three parameter sets in table 3. Set A1 is the parameter set of the previous discussions, the parameter sets A2 and A3 have larger gas temperatures T_{gas} and lower electron desorption fluxes J_{des}. The corresponding discharge current pulses and gap voltages in figure 21(a) look little different, but all are appropriate to describe the experimentally investigated discharge within a reasonable error range. For all three parameter sets, the temporal shift of the discharge current pulse minimum Δt and the change in transported charge per discharge area $\Delta\sigma$ are plotted in figures 21(b) and (c), respectively. Both show that the laser photodetachment effect is largest for the maximal assumed gas temperature. This corresponds to the parameter set with the largest reduced electric field strength $E/n = U_{gap}/(gp) \cdot k_B T_{gas}$ (gap distance g, pressure p, Boltzmann constant k_B) and the lowest electron desorption

Figure 21. Influence of the laser photodetachment depending on the laser firing time assuming negative ion formation at the cathodic dielectric ($\gamma_O^{O^-} = \gamma_{O_3}^{O_3^-} = 10^{-4}$) for different gas temperatures (compare table 3): (a) applied voltage, gap voltage and discharge current density of the unaffected discharges. (b) Temporal shift of the discharge current pulse minimum and (c) change in transported charge per area (box-shaped laser beam profile, $z_{lsr} = 1.5$ mm, $E_{lsr} = 100$ mJ) in comparison to the scaled experimental values.

Table 3. Discharge diameter, gas temperature, flux of thermally desorbed electrons and secondary electron emission coefficient for several adaptions of the simulated discharge to the experimentally investigated discharge.

Set #	$d_{dis} \times$ mm^{-1}	$T_{gas} \times$ K^{-1}	$J_{des} \times$ cm^2 s	γ_+
A1	12	300	10^{11}	0.010
A2	12	320	5×10^{10}	0.010
A3	12	350	2×10^{10}	0.005
B1	11	300	10^{10}	0.005
B2	11	300	10^{9}	0.005

flux J_{des} during the pre-phase. A larger reduced electric field strength causes a larger effective first Townsend ionization coefficient, that means a steeper increase in electron density from the cathode to the anode. This can be seen in figure 22, where the profiles of the reduced electric field strength and the electron density are plotted for the three parameter sets of figure 21 at the laser firing time of $t_{lsr} = 278$ μs. Despite the steeper increase in electron density for the larger gas temperatures, the lower electron desorption flux causes similar electron densities in the center of the gap for the three parameter sets. Therefore, the ratio of the negative ion density to the electron density is nearly the same in the center for these three parameter sets, too. Because of this, the larger reduced electric field strength for higher gas temperatures is probably
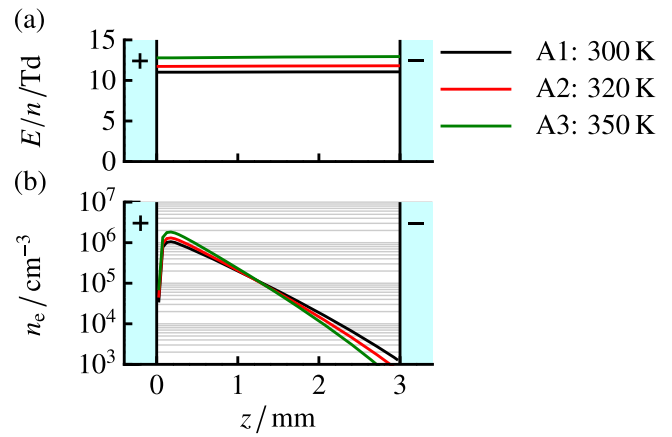

Figure 22. Axial profiles of (a) the reduced electric field strength and (b) the electron density for the parameter sets A1, A2 and A3 of table 3 under the assumption of the negative ion formation at the cathodic dielectric at $t = 278$ μs ($\gamma_O^{O^-} = \gamma_{O_3}^{O_3^-} = 10^{-4}$).

the reason for the larger laser photodetachment effect, but a clear statement is quite difficult because of the small differences in discharge current of these adapted simulated discharges.

Besides the uncertainties given from the adaption of the gas temperature, secondary electron emission coefficients, and the flux of thermally desorbed electrons, another uncertainty arises from the diameter of the discharge. It is assumed to equal the diameter of the circular electrodes of 12 mm, but since the discharge becomes inhomogeneous at the edge of the electrodes, the influence of a lower effective diameter should be taken into account. For the 1D simulation, the discharge diameter is unimportant, but the discharge diameter enters in the calculation of the gap voltage and the surface charge density from the experiment. Hence, a lower discharge diameter means a larger gap voltage in the experiment, which needs a larger breakdown voltage in the adapted simulation as well. This is shown in figure 23(a) for the parameter sets A1, B1 and B2 from table 3. As a consequence, the adapted electron desorption flux J_{des} is between one and two orders of magnitude lower than for the parameter set A1. This results in a lower electron density at the time of the laser pulse as well, which gives in turn a larger ratio of negative ions to electrons. Hence, the simulated laser photodetachment effect should be larger for the parameter sets with a diameter of 11 mm. This behavior is shown in figure 23(b) and (c), where the temporal shift of the discharge current pulse minimum Δt and the change in transported charge per discharge area $\Delta\sigma$ are plotted for the parameter sets A1, B1 and B2. As expected, the laser photodetachment effect increases for lower electron desorption fluxes J_{des}.

In summary, the adaption of the simulation to the experimentally observed discharge current and gap voltage plays a crucial role for the strength of the laser photodetachment effect. This explains why the absolute value of the laser photodetachment from the simulation agrees only partially to the experiment. Furthermore, deviations of the laser photodetachment effect from different measurement
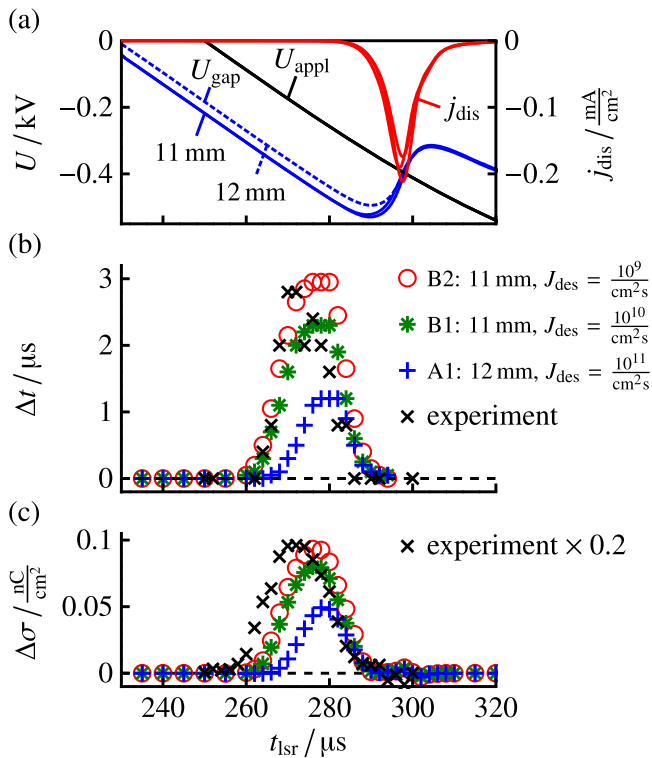
Figure 23. Influence of the laser photodetachment depending on the laser firing time assuming negative ion formation at the cathodic dielectric ($\gamma_O^{O^-} = \gamma_O^{O_3^-} = 10^{-4}$) for different discharge diameter (compare table 3): (a) applied voltage, gap voltage and discharge current density of the unaffected discharges. (b) Temporal shift of the discharge current pulse minimum and (c) change in transported charge per area (box-shaped laser beam, $z_{lsr} = 1.5$ mm, $E_{lsr} = 100$ mJ) in comparison to the scaled experimental values.

days are influenced by the changing surface properties which have large impact on the thermal electron desorption flux.

5. Conclusions

The laser photodetachment of the negative ions O^-, O_2^- and O_3^- was successfully implemented into the simulation of the helium–oxygen barrier discharge [11]. To have a measurable influence on the discharge behavior, the negative ion density has to exceed the electron density at the time of the laser pulse and the laser pulse has to take place in the late pre-phase of the discharge, because the perturbation due to the laser photodetachment has relaxation times of about 10 μs. Both conditions are not fulfilled at once by the discharge simulated with the common set of rate coefficients for electron attachment.

Therefore, two approaches are evaluated, larger electron attachment processes in the volume and the additional negative ion formation at the negatively charged dielectric surface. The first approach, the larger electron attachment in the volume, results always in a large electronegativity and a large laser photodetachment effect during the discharge current pulse. This was never observed in the experiment. Additional attachment processes or larger rate coefficients for negative

ion production in the volume cannot be responsible for the necessary large electronegativity during the discharge pre-phase. The second approach is the negative ion formation at the negatively charged dielectric by a resonant charge transfer of surface electrons to oxygen atoms or ozone molecules. It results in a larger electronegativity during the pre-phase, and the low electronegativity during the discharge current pulse remains. Therefore, this approach reproduces the dependence of the laser photodetachment effect on the variation of the laser firing time from the experiment.

Besides the variation of the laser firing time, the influence of the laser pulse energy variation on the laser photodetachment effect was studied. The good agreement with the measurement shows that the missing saturation of the laser photodetachment effect with increasing laser pulse energy is caused by the blurred laser beam profiles. The increase in laser pulse energy increases the intensity in the wings of the laser beam and causes a larger number of photodetached electrons in these areas.

A discrepancy remains between the simulated and measured axial profiles of the laser photodetachment effect. This discrepancy might be solved by introducing a time-dependent negative ion production at the dielectric surface, but this would need a description of the energy levels of the surface electrons and a measurement of the electron binding energies for comparison as well. Additionally to those studies, it is recommended to perform the laser photodetachment experiment during the first discharge breakdowns. Since the oxygen atoms and ozone molecules accumulate during several discharge pulses, this would cause lower densities of these species and negative ions during the first discharge periods.

Nevertheless, the simulation of the laser photodetachment gives important information about the influence of the electron attachment in the volume and the impact of negative ions on the discharge. In particular, volume attachment cannot be responsible for the laser photodetachment effect, and these processes are too small to have an effect on the discharge with helium and 400 ppm oxygen as well. However, the discussion shows that the negative ion formation at the negatively charged surface might increase the negative ion density in the pre-phase by several orders of magnitude. Such large negative ion densities can contribute to the release of electrons during the pre-phase by detachment processes. For large formation rates of negative ions at the negatively charged dielectric, this competes with the thermal electron desorption flux. In conclusion, the formation of negative ions at the negatively charged dielectric might be responsible for lowering the breakdown voltage and favor the diffuse discharge development.

Acknowledgments

References

[1] Fridman G, Friedman G, Gutsol A, Shekhter A B, Vasilets V N and Fridman A 2008 Applied plasma medicine *Plasma Process. Polym.* **5** 503–33

[2] Laroussi M and Leipold F 2004 Evaluation of the roles of reactive species, heat, and UV radiation in the inactivation of bacterial cells by air plasmas at atmospheric pressure *Int. J. Mass Spectrom.* **233** 86

[3] Lu X P, Ye T, Cao Y G, Sun Z Y, Xiong Q, Tang Z Y, Xiong Z L, Hu J, Jiang Z H and Pan Y 2008 The roles of the various plasma agents in the inactivation of bacteria *J. Appl. Phys.* **104** 053309

[4] Kogelschatz U 2003 Dielectric-barrier discharges: Their history, discharge physics, and industrial applications *Plasma Chem. Plasma Process.* **23** 1–46

[5] Wagner H-E, Brandenburg R, Kozlov K V, Sonnenfeld A, Michel P and Behnke J F 2003 The barrier discharge: basic properties and applications to surface treatment *Vacuum* **71** 417–36

[6] Massines F, Gherardi N, Naudé N and Ségur P 2009 Recent advances in the understanding of homogeneous dielectric barrier discharges *Eur. Phys. J. Appl. Phys.* **47** 22805

[7] Dosoudilov L, Tschiersch R, Bogaczyk M, Navrtil Z, Wagner H-E and Trunec D 2015 Investigation of helium barrier discharges with small admixtures of oxygen *J. Phys. D: Appl. Phys.* **48** 355204

[8] Bacal M 2000 Photodetachment diagnostic techniques for measuring negative ion densities and temperatures in plasmas *Rev. Sci. Instrum.* **71** 3981–4006

[9] Küllig C, Dittmann K and Meichsner J 2010 A novel approach for negative ion analysis using 160 GHz microwave interferometry and laser photodetachment in oxygen CC-RF plasmas *Plasma Sources Sci. Technol.* **19** 065011

[10] Tschiersch R, Nemschokmichal S and Meichsner J 2016 The influence of negative ions in heliumoxygen barrier discharges: I. Laser photodetachment experiment *Plasma Sources Sci. Technol.* **25** 025004

[11] Nemschokmichal S, Tschiersch R and Meichsner J 2016 The influence of negative ions in heliumoxygen barrier discharges: II. 1D fluid simulation and adaption to the experiment *Plasma Sources Sci. Technol.* **25** 055024

[12] Hagelaar G J M and Pitchford L C 2005 Solving the boltzmann equation to obtain electron transport coefficients and rate coefficients for fluid models *Plasma Sources Sci. Technol.* **14** 722

[13] Hagelaar G J M BOLSIG+ 6/2013, http://bolsig.laplace.univ-tlse.fr/

[14] Lisbon database www.lxcat.net (Accessed: August 2015)

[15] Liu D-X, Rong M-Z, Wang X-H, Iza F, Kong M G and Bruggeman P 2010 Main species and physicochemical processes in cold atmospheric-pressure He+O$_2$ plasmas *Plasma Process. Polym.* **7** 846–65

[16] Branscomb L M, Burch D S, Smith S J and Geltman S 1958 Photodetachment cross section and the electron affinity of atomic oxygen *Phys. Rev.* **111** 504–13

[17] Burch D S, Smith S J and Branscomb L M 1958 Photodetachment of O$_2^-$ *Phys. Rev.* **112** 171–5

[18] Wang L J, Woo S B and Helmy E M 1987 Laser photodetachment of O$_3^-$ *Phys. Rev.* A **35** 759–63

[19] Wong S F, Vorburger T V and Woo S B 1972 Photodetachment of O$_3^-$ in a drift tube *Phys. Rev.* A **5** 2598–604

[20] Cosby P C, Moseley J T, Peterson J R and Ling J H 1978 Photodissociation spectroscopy of O$_3^-$ *J. Chem. Phys.* **69** 2771–8

[21] Zeuner M, Meichsner J and Rees J A 1996 High energy negative ions in a radio-frequency discharge *J. Appl. Phys.* **79** 9379–81

[22] Stoffels E, Stoffels W W, Kroutilina V M, Wagner H-E and Meichsner J 2001 Near-surface generation of negative ions in low-pressure discharges *J. Vac. Sci. Technol.* A **19** 2109–15

[23] Bacal M 2006 Physics aspects of negative ion sources *Nucl. Fusion* **46** S250

[24] Belchenko Yu I, Dimov G I and Dudnikov V G 1974 A powerful injector of neutrals with a surface-plasma source of negative ions *Nucl. Fusion* **14** 113

[25] Heinisch R L, Bronold F X and Fehske H 2012 Electron surface layer at the interface of a plasma and a dielectric wall *Phys. Rev.* B **85** 075323

[26] Bronold F X, Fehske H, Heinisch R L and Marbach J 2012 Wall charge and potential from a microscopic point of view *Contrib. Plasma Phys.* **52** 856–63

[27] Ambrico P F, Ambrico M, Schiavulli L, Ligonzo T and Augelli V 2009 Charge trapping induced by plasma in alumina electrode surface investigated by thermoluminescence and optically stimulated luminescence *Appl. Phys. Lett.* **94** 051501

[28] Ambrico P F, Ambrico M, Colaianni A, Schiavulli L, Dilecce G and De Benedictis S 2010 Thermoluminescence study of the trapped charge at an alumina surface electrode in different dielectric barrier discharge regimes *J. Phys. D: Appl. Phys.* **43** 325201

[29] Li M, Li C, Zhan H, Xu J and Wang X 2008 Effect of surface charge trapping on dielectric barrier discharge *Appl. Phys. Lett.* **92** 031503

[30] Hagelaar G J M, de Hoog F J and Kroesen G M W 2000 Boundary conditions in fluid models of gas discharges *Phys. Rev.* E **62** 1452–4